Superior metal storage behavior of Zn-containing porous carbon nanostructures for Na and Li metal batteries

Kyungbae Kim,[a] Seunghwan Jeon,[b] Han-Seul Kim,[a] Hyungeun Seo,[a] Hyun-seung Kim,[b] Marca M. Doeff,[c] Sang-Gil Woo*[b] and Jae-Hun Kim*[a]

[a]School of Materials Science and Engineering, Kookmin University, Seoul 02707, Republic of Korea. E-mail: jaehunkim@kookmin.ac.kr

[b]Advanced Batteries Research Center, Korea Electronics Technology Institute, Seongnam, Gyeonggi 13509, Republic of Korea. E-mail: blackdragon@keti.re.kr

[c]Energy Storage and Distributed Resources Division, Lawrence Berkeley National Laboratory, Berkeley, CA 94720, USA

* Corresponding authors.

E-mail addresses: blackdragon@keti.re.kr (S.-G Woo), jaehunkim@kookmin.ac.kr (J.-H. Kim)

ABSTRACT

Na and Li metals are ideal anodes for high-energy rechargeable batteries. However, their poor Coulombic efficiency and the associated safety issues due to dendritic metal deposition and large volume changes during the metallic plating/stripping are the major causes that persistently hinder their practical energy-storage applications. Herein, Zn-containing carbon nanostructures derived from the typical zeolitic imidazolate framework-8 (ZIF-8) are proposed as advanced metal anode materials for both Na and Li metal batteries. The three-dimensional interconnected porous surfaces confine metallic Na and Li within the nanostructures, filling the carbon scaffold, and covering the electrode surface to form stable solid electrolyte interphases. Based on the metal nucleation and growth results obtained through various electrochemical tests, Zn incorporation and pore morphology have been revealed as the key factors that regulate the metal nucleation and metallic plating/stripping during the cycling. Thus, the incorporation of Zn in the closed pores of a carbon nanostructure improves the cycle performance, even in carbonate electrolytes, and produces stable Na and Li metallic anodes for next-generation rechargeable batteries.

KEYWORDS: Na metal battery; Li metal battery; anode; Zeolitic imidazolate framework; Zn-containing porous carbon

1. Introduction

Li-based rechargeable batteries are dominantly used in most portable and small-sized electronic devices, and are being rapidly developed for large-scale energy storage in electric vehicles and grids. The increasing market demands for such advanced devices have accelerated the research on the fabrication of high-energy-density batteries.[1, 2] To increase the energy density, the key is to develop high-capacity anode and cathode materials.[3, 4] In this direction, metallic Li anodes have extensively studied owing to the incomparably high theoretical capacity (3860 mAh g^{-1}) and low redox potential (–3.04 V vs. standard hydrogen electrode (SHE)).[5, 6] However, its application is limited by several shortcomings such as Li dendrite growth and associated safety hazards.[7-9] Furthermore, Na-based batteries have garnered extensive attention because of the high theoretical capacity (1166 mAh g^{-1}) and low redox potential (–2.71 V vs. SHE) of Na anodes.[10] In particular, metallic Na exhibits electrochemical properties (voltage profiles and cycling stability) comparable to those of Li metal, but has a much higher natural abundance, and is cheaper, rendering it suitable for battery applications where cost and sustainability are important, as an alternative to Li.[11-13]

Similar to the Li metal anodes, Na metal anodes also exhibit two drawbacks, *viz*. inability to overcome cyclability and safety issues, which intrinsically originate from their high chemical reactivity and large volume change, during the metal deposition.[14] The high chemical potential of Na metal induces a heterogeneous nucleation with a continuous flow of metal ions through the electrolyte, thereby generating an uncontrolled dendritic metal growth on the electrode surface (Fig. 1a).[15] In addition, the large volume change during Na metal deposition occurs because there is no encapsulating host, resulting in formation of “dead” Na from the physical loss of the active material, which, in turn, leads to capacity degradation.[16] To overcome these challenges, significant research efforts have devoted to the development

of feasible strategies for stabilizing Na.[14-19] Among these methods, the one involving artificially designed three-dimensional (3D) host structures has been mainly developed and investigated for stable Na metallic plating/stripping.[20-22] However, most reported studies are focused on the morphology of metallic Na, and the investigation on the initial nucleation process has rarely been explored.

Reportedly, the nucleation of alkali metal depends on the chemical potential of metal and geometry of the metal substrates.[23] To modify the substrate surfaces, carbonaceous materials have been considered a promising candidate owing to their electrical conductivity and processability. Although they could be energetically suitable candidates for the deposition of metallic Na rather than planar metal substrates,[24] not all carbon structures are suitable for storing Na. Even on a nanostructured carbon, the Na^+ ion flux can be easily localized, leading to a dendritic growth.[11, 12] To control the uniformity of Na nucleation, enhancing the Na-storage properties of carbonaceous materials via elaborate design of carbonaceous matrices with surface modifications, such as those containing conducting mesopores,[25] defects,[26] and specific Na-inactive/active heteroatom dopants,[27-29] has been demonstrated as a feasible method in various previously reported studies. The 3D carbonaceous matrices with large surface areas enable a uniform Na plating in the carbon structures by reducing the nucleation overpotential and local current density. Notably, transition metals (e.g., Fe, Co, Ni, Cu, Zn), noble metals (e.g., Au, Ag), and heteroatoms (e.g., N, P, S) can effectively regulate the Na plating in an enclosed microstructure. Furthermore, we may consider that the chemical reactivity of Na can be controlled by sodiophilic site coordination in a carbon matrix at various concentrations. Therefore, combining these methods can be a simple and effective strategy for dispersing the sodiophilic sites and incorporating conductive heteroatoms in the host matrix.

In this study, we investigated the effect of Na-nuclei-favorable metal incorporation into a 3D interconnected carbon structure for achieving a stable metal deposition and dissolution cycle. Zeolitic imidazolate frameworks-8 (ZIF-8) have been used recently to prepare Zn-incorporated porous carbon structures. Generally, Zn-based materials such as Zn_4Sb_3 and $ZnSnO_3$ are considered to be conversion-type compounds for Na storage, because of the low solubility of metallic Zn with Na. The $NaZn_{13}$ phase has a low theoretical capacity (31 mAh g^{-1}) at the fully charged state, as determined from a Zn–Na phase diagram.[30, 31] Therefore, Zn was selected as the Na-nuclei-favorable metal in this study, because it can induce Na metal nucleation without high degrees of electrochemical Zn-Na alloying reaction. To evaluate the effect of Zn incorporation on the porous carbon structure, we carefully controlled the Zn concentration in the carbon materials, through chemical etching. As a result, the Zn nanoparticles were uniformly incorporated, with different contents, into porous carbon materials derived from ZIF-8. The Zn nanoparticles are expected to play an important role in enhancing the affinity between Na and the carbon surface, thus reducing the metal nucleation overpotential and regulating the stable metal plating/stripping (Fig. 1b). The prepared materials were also tested for Li metal electrodes, and the corresponding results were compared with those of the Na metal storage. This highly controlled porous structure could induce uniform dispersion of the electrons, thereby reducing the extremely high local current density to suppress the dendritic growth of both Na and Li. Full-cell type batteries were successfully tested, demonstrating the outstanding cycle and rate performances of the fabricated electrodes.

2. Experimental

Synthesis of ZIF-derived Zn-containing porous carbon

Zinc acetate dihydrate ($Zn(CH_3COO)_2 \cdot 2H_2O$, 0.66 g; Sigma-Aldrich), 2-methylimidazole ($C_4H_6N_2$, 1.95 g; Sigma-Aldrich), and polyvinylpyrrolidone (PVP, 0.15 g; Sigma-Aldrich) were separately dissolved in a methanol solution (60 mL) under sonication for 10 min. All the prepared solutions were mixed in a closed vial using magnetic stirring for 10 min and then statically aged at 25 °C for 24 h in a thermostatic oven. The aged white solution was washed several times with methanol using a centrifuge, and the obtained white precipitates were vacuum-dried at 80 °C for 24 h to prepare the ZIF-8 nanoparticles. Finally, the resulting as-prepared ZIF-8 nanoparticles were transferred into a quartz boat inside a horizontal furnace and heat-treated at 600 °C (heating rate: 2 °C min^{-1}) for 5 h in an N_2 atmosphere for carbonization. To regulate the Zn content in the ZIF-derived carbon, the nanoparticles were chemically etched, with a 2 M HCl solution, for 2 and 5 h.

Materials characterization

The surface morphology and microstructure of the ZIF-derived porous carbon materials were characterized by field-emission scanning electron microscopy (FE-SEM; JEOL 7500) and high-resolution transmission electron microscopy (HR-TEM; Talos F200X) combined with energy dispersive spectroscopy (EDS). The crystal structures of the synthesized materials were determined by X-ray diffraction (XRD; Rigaku D/Max-2500V). X-ray photoelectron spectroscopy (XPS; Thermo Scientific), Raman (Bruker SENTERRA), and Fourier transform infrared (FT-IR; Bruker VERTEX 70) spectroscopies were performed to analyze the binding energies of the constituent elements as well as the bonding structure of the materials. The Brunauer–Emmett–Teller (BET) surface areas and pore volumes of the porous carbon materials were analyzed through N_2 physisorption (Micromeritics TriStar II 3020). The

metallic Zn content in the synthesized materials was evaluated by inductively coupled plasma-mass spectroscopy (ICP-MS, Agilent 7900).

Electrode preparation

The ZIF-derived Zn-containing porous carbon electrodes were prepared through a simple slurry-cast method. The synthesized materials were mixed with a polyacrylic acid (PAA, Sigma-Aldrich) binder (1:1 by weight) in deionized water to form slurries, which were then cast onto cleaned Cu foils using a doctor blade with a height of 25 μm. The slurry-casted electrodes were dried in an oven at 80 °C for 6 h and then vacuum-dried at 100 °C for 24 h. The electrodes were cut into coin-type disks each with a diameter of 12 mm for the half-cells and 14 mm for the full cells. The areal mass loading and thickness of the host materials were approximately 2 mg cm^{-2} and 18 μm, respectively. Two cathodes were prepared for the Li and Na full-cell tests. Commercially available lithium cobalt oxide ($LiCoO_2$, denoted as LCO; Umicore) and laboratory-synthesized sodium cobalt oxide ($Na_{0.71}CoO_2$, denoted as NCO) powders were mixed with a conducting agent (Super P, Timcal) and polyvinylidene fluoride (PVDF; Kynar 2801) binder (8:1:1 in weight ratio) in N-methyl-2-pyrrolidone (Samchun Chemicals). The slurries were coated onto Al foils and dried in an oven at 120 °C for 3 h. The dried electrodes were roll-pressed and then vacuum-dried at 120 °C for 24 h. The electrodes were cut into coin-type disks each with a diameter of 12 mm. The average mass loadings of the active material were approximately 6.7 and 9.7 mg cm^{-2} for LCO and NCO, respectively.

Electrochemical measurements

All the coin cells were assembled with standard CR2032-type cells in an Ar-filled glove box containing moisture and oxygen with concentration below 1 ppm. Na and Li metal foils were used as the counter/reference electrodes, and polyacrylonitrile/polyethylene terephthalate/polyacrylonitrile layered films were employed as separators. For the Na cells, 1 M $NaPF_6$ was dissolved in ethylene carbonate/propylene carbonate/fluorobenzene (4:4:2 in volume ratio; Panax Etec) containing 2wt% fluoroethylene carbonate (FEC) to prepare the carbonate-based electrolyte. For the Li cells, 1 M $LiPF_6$ dissolved in ethylene carbonate/diethyl carbonate (3:7 in volume ratio) containing 10wt% FEC was used as the electrolyte. Galvanostatic Li/Na plating and stripping tests were performed in a battery cycler (Basytec CTS-Lab). For the first cycle, a fixed amount of Na and Li (capacity: 2 mAh cm^{-2}) were plated and stripped at a current density of 0.1 mA cm^{-2}. For long-term cycling of the half-cells, the first deposition capacity was 2 mAh cm^{-2}, and the subsequent metallic plating/stripping were fixed at 1 mAh cm^{-2}. Cleaned Cu foils were tested using the same process for comparison. The rate capability test was performed with various constant current densities between 0.1 to 15 mA cm^{-2}. All the half-type cell tests were carried out in the voltage rage of –2.0 to 2.0 V vs. Na^+/Na and Li^+/Li at 25 °C in a thermostatic oven. The full-cell tests were performed only with the carbonate electrolyte with each pair of cathodes. The anodes were pre-deposited with 2 mAh cm^{-2} for both Na and Li. The voltage ranges for Na and Li full-cells were 2.0–3.8 V and 3.0–4.3 V, respectively.

3. Results and discussion

In this study, we designed and prepared 3D interconnected porous carbon structures with uniformly incorporated Zn particles through the pyrolysis of ZIF-8. The Zn contents in the

porous carbon were varied by adjusting the chemical etching time. Three types of materials were prepared, denoted as high Zn-containing porous carbon (HZPC, without etching), medium Zn-containing porous carbon (MZPC, etching for 2 h), and low Zn-containing porous carbon (LZPC, etching for 5 h). Fig. 2a shows a clear rhombic dodecahedral ZIF-8 nanoparticle morphology with a particle size of approximately 400 nm for the HZPC sample. The schematic illustration of the synthesis process and morphology changes are presented in Fig. S1a. Micropores that were generated during the carbonization of the as-prepared ZIF-8 remained on the sample surfaces even after the HCl-mediated chemical etching of all the samples (Fig. S1b–i). The high-magnification TEM images show the modified interfaces with micropores and mesopores, maintaining the rhombic dodecahedral carbon structure in the HZPC nanostructure (Fig. 2b,c). The selected area electron diffraction pattern of HZPC indicates that the carbon is in an amorphous state (Fig. 2c inset). Fig. 2d presents the HR-TEM image showing the existence of Zn clusters in the closed pores of HZPC. The XRD pattern of the as-prepared ZIF-8 (Fig. S2) is consistent with the previously reported crystal structure of the ZIF-based materials.[32]

After the heat treatment, significant peak broadening was observed at 16° and 24°, and a small peak observed at 8.5° could be attributed to the long-range ordered crystalline structures. These results indicate that the structure partly collapsed, with broken coordination bonds between Zn^{2+} and organic ligands, into a short-ranged order because of carbonization.[33] Furthermore, several cavities and pore clusters belonging to the core were observed in the internal microstructure of the rhombic dodecahedron-shaped carbon as shown in the scanning TEM (STEM) images with the EDS elemental line scan results in Fig. 2e. This pore distribution of the HZPC structure was observed in the low magnification STEM images (Fig. S3). The EDS elemental mapping results revealed the presence of C, Zn, and N, with uniform

elemental distributions, after the carbonization under N_2 atmosphere (Fig. 2f–h). It was confirmed that N was incorporated into the carbon structure, and according to the previously reported studies, N incorporation increases the electrical conductivity of the structure.[28] As the etching times increased, the same rhombic dodecahedral morphology with a uniform elemental distribution was observed for both the MZPC and LZPC samples (Fig. S4 and S5). However, the internal morphologies (no core pores) of these samples showed slight differences (Fig. S4 and S5) because of the HCl treatment, which caused a partial physical exfoliation of the carbon scaffold and Zn removal

To further examine the HZPC sample, additional material characterizations were performed. The schematic illustration of the synthesized materials, based on the TEM and EDS analyses, is shown in Fig. 3a. The BET surface areas and total pore volumes with pore size distributions were examined through the N_2 adsorption/desorption analysis (Fig. 3b). The N_2 isotherms of HZPC show type I and IV plateaus with a hysteresis loop at high relative pressures (at 0.99 P/P_0), indicating a uniform micropore distribution (inset Fig. 3b). Moreover, the N_2 isotherms and pore size distributions of the as-prepared ZIF-8, MZPC, and LZPC are also compared in Fig. S6. The profiles are similar to that of HZPC, but the average pore size increases with decreasing Zn content. Table 1 shows the specific surface areas, total pore volumes, average pore sizes, and Zn contents (measured by ICP-MS) of the samples. Noticeably, LZPC exhibits a higher specific surface area and two times higher total pore volume than HZPC. The increased etching time induced additional removal of Zn along with surface exfoliation, thereby increasing the surface area and internal pore volume. This result is in good agreement with those of the FE-SEM and HR-TEM analyses. The Zn contents of the HZPC, MZPC, and LZPC samples were measured to be approximately 23.7wt%, 14.8wt %, and 5.26wt%, respectively.

Table 1. Physical characterization results of porous carbon structure derived from ZIF-8.

Materials	Specific surface area ($m^2\ g^{-1}$)	Total pore volume ($cm^3\ g^{-1}$)	Average pore size (nm)	Zn content ICP (wt%)
HZPC	821.5	0.550	2.681	23.7
MZPC	876.2	0.589	3.063	14.8
LZPC	901.8	1.21	5.366	5.26

The carbon bonding structure of HZPC was characterized by Raman spectroscopy, and the corresponding spectrum is presented in Fig. 3c, which shows the D and G bands at 1322 and 1585 cm^{-1}, respectively. The intensity ratio (I_D/I_G) was calculated to be 0.851, indicating that the carbon is in the amorphous state with a disordered structure.[33, 34] The band centered at 1424 cm^{-1} is attributed to the C–H wag in the methyl group, shifting from the C=C stretching vibration in the imidazolate ring.[35] These band features can be attributed to the interstitial defects that originated due to the Zn–N removal from the carbon structure.[33, 35]

The chemical states of the ZIF-derived porous carbon materials were examined by XPS. Fig. 3d–f show the core-level XPS spectra of the HZPC sample before and after Ar-ion etching for 600 s. For comparison, XPS spectra of all the synthesized materials are presented in Fig. S7. Fig. 3d shows the C 1s core-level spectrum with deconvoluted sub-profiles. For both the before and after Ar-ion cleaning cases, a sub-profile attributable to the C–C bond is observed at a binding energy of 284.8 eV with the highest relative intensity. Compared to the as-prepared ZIF-8 material (Fig. S7a), the carbonized samples show a peak shift from 285.5 to 284.8 eV, indicating the transformation of sp^2 C=N to a pure carbon.[33] Furthermore, peaks corresponding to C–N, C–O, and C=O are also observed at higher binding energies.[33, 36, 37]

Fig. 3e shows the Zn 2p core-level XPS spectrum of the HZPC sample. The observed deconvoluted sub-profiles of the sample before the etching could be ascribed to the chemical bonding structures of zinc acetate, hydroxide, and carbonate.[38] After the Ar-ion etching, the peaks corresponding to $2p_{3/2}$ and $2p_{1/2}$, observed at binding energies of 1021.7 and 1044.7 eV, respectively, shift to the lower binding energy side by approximately 4.0 eV. This indicates that the profiles correspond to metallic Zn instead of Zn–O. A binding energy difference of 23 eV between $2p_{3/2}$ and $2p_{1/2}$ is measured, indicating that metallic Zn clusters were confined inside the micropores and carbon host structure.[39] The intensities of the Zn 2p profiles of MZPC and LZPC significantly decrease with decreasing Zn concentration (removal of Zn clusters via chemical etching; Fig. S7b).

The N 1s XPS spectra are displayed in Fig. 3f. Before the Ar-ion etching, four deconvoluted sub-profiles were observed, which could be assigned to pyridinic N (398.5 eV), pyrrolic N (400.0 eV), quaternary N (401.6 eV), and oxidized N (404.0 eV) [33, 40-42]. After the ion etching, the large contribution of the oxidized N almost disappeared, as evident from the organic ligands pyrolyzed in the ZIF-8 structure. The intensities of the three deconvoluted peaks of pyridinic N, pyrrolic N, and quaternary N significantly increased along the relatively narrow spectrum split, providing evidence of the partially broken Zn–N bond and the strong C=N bond structures indicated in the FT-IR spectra shown in Fig. S8. This indicates that the as-prepared ZIF structure was maintained after the carbonization.[33] After the chemical etching treatment, the intensities of the N 1s profiles of MZPC and LZPC were reduced (Fig. S7c). It could be considered that the N-doped graphitic carbon was etched out with the metallic Zn removal. These results clearly demonstrate that the carbon structure with uniform and stable closed pores can contain a large number of Zn clusters. Therefore, Zn was well

dispersed and incorporated into the porous carbon structures with confined pore textures engineered in this study.

To investigate the electrochemical behavior during the nucleation, growth, and plating/striping of Na, electrochemical cycling tests were galvanostatically performed on all the Zn-containing porous carbon electrodes and bare Cu foils to compare the role of Zn clusters in the carbon structure. These tests were also performed for Li. The presence of conducting materials and binder could be crucial for improving the initial metal nucleation on the Zn-containing electrodes. We only used active materials and the PAA binder to achieve a higher film adhesion to current collectors and to minimize interfacial side reactions between the active ions (Na^+ and Li^+) and other additives. The electrical conductivity of the electrodes was measured and the results are given in Table S1.

The metal deposition was performed with a fixed capacity of 2 mAh cm^{-2} at a constant current density of 0.1 mA cm^{-2} in the carbonate-based electrolyte, and the corresponding first voltage profiles are shown in Fig. 4a. The Coulombic efficiencies of the HZPC, MZPC, and LZPC electrodes are 97 %, 88 %, 86 %, respectively, and that for the bare Cu current collector is 83%. The HZPC electrode exhibits the highest efficiency possibly because of the Zn incorporation effect. Two distinguishable parts of the overpotential are observed in the voltage profiles. One part is nucleation overpotential (η_n), which relates to a sharp potential dip at the onset of metal deposition. The other part is the plateau overpotential (η_p), which is affected by the continuous transfer of the metal ions from the electrolyte for further metal growth and plating as the potential increases with time.[18, 24] The enlarged voltage profiles of the overpotential dips are represented in Fig. 4a (inset). The bare Cu-foil electrode exhibits a sharp potential dip at –0.247 V (vs. Na^+/Na) for Na nucleation because of the large thermodynamic mismatch between Na and Cu for the heterogeneous nucleation of Na.[24]

Then, the potential rises and exhibits a relatively flat profile with deposition. The η_p of the bare Cu electrode is measured to be 0.052 V. The η_n is the difference between the potential dip and η_p, and it is 0.195 V for the bare Cu electrode. For the porous carbon electrodes, both η_n and η_p are much lower. The values are 0.054 and 0.041 V (HZPC); 0.100 and 0.046 V (MZPC); 0.162 and 0.050 V (LZPC), respectively. The Zn-containing porous carbon electrodes exhibit significantly lower η_n values, indicating the Zn clusters can facilitate the nucleation of Na on the porous carbon.[43, 44] As the Zn content increases, the nucleation overpotential decreases. The HZPC electrode shows the smallest value, which supports the role of Zn clusters for facilitating Na nucleation. The η_n and η_p overpotentials of the HZPC and bare Cu foil electrodes at various current densities from 0.1 to 10 mA cm^{-2} are shown in Fig. 4b. The voltage profiles and related explanation are presented in Fig. S9. The HZPC electrode exhibits much lower overpotentials than the bare Cu electrode at higher current densities.

To investigate the effect of Zn on the nucleation, we carefully compared the electrochemical properties of the Zn powder electrodes for Na and Li storage (Fig. S10). The Zn powder and a binder (PAA or PVDF) were used to prepare electrode slurries, where the number means the percent ratio of the binder (or activated carbon). Metallic Zn powder electrodes were found to be more favorable as assistant materials for Na deposition (Fig. S10a), whereas they were electrochemically alloyed with Li to form a LiZn phase after full lithiation (Fig. S10d) as reported previously.[45, 46] Comparing these two cases shows that Zn can be used as an assistant material, without electrochemical alloying, for the facile nucleation of Na, and the well-dispersed Zn clusters in a porous carbon structure can accelerate the Na nucleation. However, for Li deposition, Zn can be electrochemically alloyed with Li causing reactions, following which the Li deposition can start. The voltage

profiles and cycle performance of the Zn electrodes used for Na and Li deposition and dissolution cycling are depicted in Fig. S10. In both cases, the cycle performance degrades as the cycle number increases, indicating that only using Zn powder electrodes is not suitable for Na cycling and the Li–Zn alloying reactions are not appropriate for Li storage. Therefore, the porous carbon framework can play an important role in achieving long-term Na storage, and the Zn clusters can accelerate the Na nucleation with the carbon material. The voltage profiles of all the Zn-containing porous carbon electrodes for Li storage at various current densities are presented in Fig. S11 and S12 for comparison. Differences in overpotentials are similarly observed according to the Zn content in the porous carbon.

To examine the role of the Zn metal clusters for Na metal plating, the morphology of the HZPC electrodes was analyzed via ex situ FE-SEM with EDS elemental mapping analysis at a charge level of 1.0 mAh cm^{-2} (Fig. 4c–f). The FE-SEM images of the electrode at various charge states of 0.2, 1.0, 2.0, and 4.0 mAh cm^{-2} are shown in Fig. S13. Na deposition could be induced on the sodiophilic sites of the Zn clusters because of the $NaZn_{13}$ phase. The Na-Zn alloying could be detected from the voltage profiles. This initial Na nucleation could occur at a charge state of 0.2 mAh cm^{-2}. As the charge level increased to 1.0 and 2.0 mAh cm^{-2}, the metallic Na could further grow. However, the surface morphology of the electrodes is similar. Furthermore, the cross-sectional FE-SEM images of the pristine electrode (Fig. S14) and charged electrode (2.0 mAh cm^{-2}, Fig. S15) showed almost the same electrode thickness. This indicates that the Na nucleation possibly initiates inside the pores on the Zn clusters, and further metal growth inside the porous carbon structure can be regulated. In contrast, a different morphology is observed in the Li system with increasing charge level (Fig. S16). At a charge state of 0.2 mAh cm^{-2}, a similar morphology is observed, indicating that the Li nucleation initiates inside the pores. However, the surface morphology changes with metallic

Li deposition as the charge level is increased to 1.0, 2.0, and 4.0 mAh cm^{-2}. This can be attributed to the different nucleation behavior of Li. In the case of Li deposition, the Li nucleation on the outside surface of the porous carbon occurs easily as well, and thus, both internal and external Li growth can be obtained. This different metal growth behavior that can affect the electrochemical performance is observed for Na and Li deposition.

To evaluate the cycle performance of the porous carbon electrodes for Na, galvanostatic long-term plating/stripping tests were performed with an initial charge capacity of 2.0 mAh cm^{-2}, and the subsequent discharge and charge capacity was fixed at 1.0 mAh cm^{-2} with a current density of 1.0 mA cm^{-2}. Fig. 5a shows the voltage profiles of the HZPC electrode, acquired for 5500 h. As the cycle number increases, the overpotential slightly increases for deposition and dissolution. However, the cycling performance is well maintained up to approximately 3000 cycles. The enlarged voltage profiles at the selected positions of the 250^{th} cycles are presented in the inset. For the 250^{th} cycles, the reference bare Cu foil electrode shows a high potential difference between deposition and dissolution, whereas all the ZPC electrodes exhibit similar low overpotentials. The HZPC electrode test results (at the 1000^{th}, 2000^{th}, and 3000^{th} cycles), included in the insets, show stable voltage profiles with uniform overpotentials. The corresponding ex situ FE-SEM images after the cycles are represented in Fig. 5b–e. A similar morphology of the HZPC electrode surface is maintained after the 1000^{th} deposition (Fig. 5b). After the 2000^{th} deposition, the porous carbon is covered with Na, including solid electrolyte interphase films (Fig. 5c). Although this bulk metal is removed after the 2000^{th} dissolution (Fig. 5d), a bulky metal morphology is again observed after 3000 cycles (Fig. 5e).

Fig. 5f shows the Coulombic efficiency of all the Zn-containing porous carbon and Cu foil electrodes with increasing cycle number. The Coulombic efficiency of the HZPC

electrode is well maintained up to 2800 cycles, whereas those of the MZPC, LZPC, and bare Cu foil electrodes dropped rapidly after 415, 312, and 267 cycles, respectively. This indicates that the increased Zn content can be helpful for improving the long-term cycling performance. The rate capability of the HZPC electrode is shown in Fig. 5g, indicating that the overpotential increases with the increasing current density; however, the values were not very high even at high current densities of 10 mA cm^{-2}. Additionally, when the current density returns to 1 mA cm^{-2}, the previous voltage profiles are almost fully recovered. Furthermore, the long-term cycling for high-rates of 10 mA cm^{-2} was also performed (Fig. S17). The cycling performance at 10 mA cm^{-2} was well maintained over 3000 cycles. This means that the designed Zn-containing porous carbon structure is suitable for the facile and fast deposition and dissolution of Na.

The electrochemical tests were also performed for the Li system, under the same conditions. Fig. S18 shows the comparison of the voltage profiles for all the electrodes. The HZPC electrode shows a stable long-term cycling performance with a gradually increasing overpotential over 1500 cycles. However, the deposited Li exhibited different morphologies after the long-term cycling (see the FE-SEM images in Fig. S18b–e); that is, a noticeable dendritic Li growth is observed, and these dendrites remain even after the Li stripping at the same cycles (1200th cycle, see Fig. S18c, d). In the first cycle, the Li–Zn alloy can be formed, inducing a large volume expansion inside the Zn-containing porous carbon. During further Li deposition after the long cycles, some surface pores partially collapse due to the dendritic colony on the carbon structure. Nevertheless, further dendrite growth can occur and, finally the Coulombic efficiency rapidly decreases after approximately 1600 cycles (Fig. S18e). In contrast, no dendrite growth is observed in the Na system (Fig. 5b–e). This

difference can be attributed to the different applications of the Zn-containing porous carbon structure to both Na and Li storage.

To examine the feasibility of the HZPC electrodes in practical energy storage applications, full-cell tests were carried out using the synthesized NCO and the commercial LCO cathodes against the pre-deposited HZPC anodes. NCO was synthesized using a solid-state method with heat treatment, and the corresponding XRD pattern is shown in Fig. S19. The initial voltage profiles of both the Na and Li half cells are presented in Fig. S20. The rate at various current densities of 0.1–5.0 C and the cycle performances at 0.1 and 1.0 C of the Na full cells are displayed in Fig. 6. The Na full cell exhibits a remarkable rate performance (Fig. 6a). A discharge capacity of 99 mAh g^{-1} is obtained at 0.1 C, and a capacity of 75 mAh g^{-1} is maintained at 5.0 C. The voltage profiles at various rates are shown in Fig. 6b, revealing the typical features of NCO along with the increase in the overpotentials with increasing rates.[47] Fig. 6c shows the cycling performance of the Na full cells. Evidently, the reversible capacity can be well maintained after 100 cycles. Notably, the cycling performance of the Na full cells with the HZPC electrode is superior to those of the previously reported ZIF-derived electrode materials, and the comparison of these materials is shown in Table S2. The electrochemical properties of the Li full cells are presented in Fig. S21. For comparison, the electrochemical performance of full cells including the LZPC electrode is also shown in Fig. S22. The Na and Li full cell results reflect the feasibility of HZPC anodes as efficient and high-performance materials for the development of practical and next generation high-energy rechargeable battery systems.

4. Conclusions

In this study, we successfully demonstrated the effect of Zn incorporation into 3D porous carbon materials. Zn-containing porous carbon structure scaffolds were derived from ZIF-8 through a simple precipitation and pyrolysis carbonization with additional chemical treatments. The 3D interconnected porous surface confined metallic Na and Li within its nanostructure, such that these metal particles filled the carbon scaffold as well as covered the entire electrode surface forming stable solid electrolyte interphases. As the Zn content increased, the Na deposition and dissolution cycling performance improved. This enhancement in the cycling performance could be attributed to the role of Zn in realizing a stable nucleation. In addition, the effect of Zn incorporation was more evident for Na storage than in Li storage possibly because of the different electrochemical properties of Na and Li with Zn. It is demonstrated that the Zn incorporation in a porous carbon structure improves the cycle performance, even in carbonate electrolytes, and can be helpful for the development of stable Na and Li metallic anodes for next-generation rechargeable batteries.

Acknowledgments

This work was supported by the National Research Foundation of Korea (NRF) Grant funded by the Ministry of Science and ICT, Republic of Korea (2021M3H4A3A02086910, 2022R1A5A7000765, and 2022R1A2C1011181). This work was also supported by the Korea Evaluation Institute of Industrial Technology (KEIT), which is funded by the Ministry of Trade, Industry & Energy, Republic of Korea (No. 20016018). The contributions of MMD were supported by the Assistant Secretary for Energy, Efficiency and Renewable Energy, Office of Vehicle Technologies of the U.S. Department of Energy under Contract No. DE-AC02-05CH11231. This document was prepared as an account of work sponsored by the

United States Government. While this document is believed to contain correct information, neither the United States Government nor any agency thereof, nor the Regents of the University of California, nor any of their employees, makes any warranty, express or implied, or assumes any legal responsibility for the accuracy, completeness, or usefulness of any information, apparatus, product, or process disclosed, or represents that its use would not infringe privately owned rights. Reference herein to any specific commercial product, process, or service by its trade name, trademark, manufacturer, or otherwise, does not necessarily constitute or imply its endorsement, recommendation, or favoring by the United States Government or any agency thereof, or the Regents of the University of California. The views and opinions of authors expressed herein do not necessarily state or reject those of the United States Government or any agency thereof or the Regents of the University of California.

References

1. J. M. Tarascon and M. Armand, *Nature*, 2001, **414**, 359-367.
2. C.-M. Park, J.-H. Kim, H. Kim and H.-J. Sohn, *Chem. Soc. Rev.*, 2010, **39**, 3115-3141.
3. N. Nitta, F. Wu, J. T. Lee and G. Yushin, *Mater. Today*, 2015, **18**, 252-264.
4. P. Simon and Y. Gogotsi, *Nat. Mater.*, 2008, **7**, 845-854.
5. H. Kim, G. Jeong, Y.-U. Kim, J.-H. Kim, C.-M. Park and H.-J. Sohn, *Chem. Soc. Rev.*, 2013, **42**, 9011-9034.
6. Y. Zhang, T.-T. Zuo, J. Popovic, K. Lim, Y.-X. Yin, J. Maier and Y.-G. Guo, *Mater. Today*, 2020, **33**, 56-74.
7. X.-B. Cheng, R. Zhang, C.-Z. Zhao and Q. Zhang, *Chem. Rev.*, 2017, **117**, 10403-10473.
8. D. Lin, Y. Liu and Y. Cui, *Nat. Nanotechnol.*, 2017, **12**, 194-206.
9. M. D. Tikekar, S. Choudhury, Z. Tu and L. A. Archer, *Nat. Energy*, 2016, **1**, 16114.
10. B. L. Ellis and L. F. Nazar, *Curr. Opin. Solid State Mater. Sci.*, 2012, **16**, 168-177.
11. H. Wang, E. Matios, J. Luo and W. Li, *Chem. Soc. Rev.*, 2020, **49**, 3783-3805.
12. N. Yabuuchi, K. Kubota, M. Dahbi and S. Komaba, *Chem. Rev.*, 2014, **114**, 11636-11682.
13. S.-W. Kim, D.-H. Seo, X. Ma, G. Ceder and K. Kang, *Adv. Energy Mater.*, 2012, **2**, 710-721.
14. Y. Zhao, X. Yang, L.-Y. Kuo, P. Kaghazchi, Q. Sun, J. Liang, B. Wang, A. Lushington, R. Li, H. Zhang and X. Sun, *Small*, 2018, **14**, 1703717.
15. B. Lee, E. Paek, D. Mitlin and S. W. Lee, *Chem. Rev.*, 2019, **119**, 5416-5460.

16. Y. Zhao, K. R. Adair and X. Sun, *Energy Environ. Sci.*, 2018, **11**, 2673-2695.
17. S. Komaba, W. Murata, T. Ishikawa, N. Yabuuchi, T. Ozeki, T. Nakayama, A. Ogata, K. Gotoh and K. Fujiwara, *Adv. Funct. Mater.*, 2011, **21**, 3859-3867.
18. H. Liu, X.-B. Cheng, Z. Jin, R. Zhang, G. Wang, L.-Q. Chen, Q.-B. Liu, J.-Q. Huang and Q. Zhang, *EnergyChem*, 2019, **1**, 100003.
19. X. Zheng, H. Fu, C. Hu, H. Xu, Y. Huang, J. Wen, H. Sun, W. Luo and Y. Huang, *J. Phys. Chem. Lett.*, 2019, **10**, 707-714.
20. W. Luo, Y. Zhang, S. Xu, J. Dai, E. Hitz, Y. Li, C. Yang, C. Chen, B. Liu and L. Hu, *Nano Lett.*, 2017, **17**, 3792-3797.
21. D. Lin, Y. Liu, Z. Liang, H.-W. Lee, J. Sun, H. Wang, K. Yan, J. Xie and Y. Cui, *Nat. Nanotechnol.*, 2016, **11**, 626-632.
22. T.-S. Wang, Y. Liu, Y.-X. Lu, Y.-S. Hu and L.-Z. Fan, *Energy Storage Mater.*, 2018, **15**, 274-281.
23. M.-H. Ryou, Y. M. Lee, Y. Lee, M. Winter and P. Bieker, *Adv. Funct. Mater.*, 2015, **25**, 834-841.
24. Y. Deng, J. Zheng, A. Warren, J. Yin, S. Choudhury, P. Biswal, D. Zhang and L. A. Archer, *Adv. Energy Mater.*, 2019, **9**, 1901651.
25. N. Mubarak, M. Ihsan-Ul-Haq, H. Huang, J. Cui, S. Yao, A. Susca, J. Wu, M. Wang, X. Zhang, B. Huang and J.-K. Kim, *J. Mater. Chem. A*, 2020, **8**, 10269-10282.
26. W. Liu, P. Li, W. Wang, D. Zhu, Y. Chen, S. Pen, E. Paek and D. Mitlin, *ACS Nano*, 2018, **12**, 12255-12268.
27. H. Wang, E. Matios, C. Wang, J. Luo, X. Lu, X. Hu, Y. Zhang and W. Li, *J. Mater. Chem. A*, 2019, **7**, 23747-23755.
28. J. Wu, Z. Pan, Y. Zhang, B. Wang and H. Peng, *J. Mater. Chem. A*, 2018, **6**, 12932-12944.
29. Z. Li, C. Bommier, Z. S. Chong, Z. Jian, T. W. Surta, X. Wang, Z. Xing, J. C. Neuefeind, W. F. Stickle, M. Dolgos, P. A. Greaney and X. Ji, *Adv. Energy Mater.*, 2017, **7**, 1602894.
30. Y. Liu, Y. Ge and D. Yu, *J. Alloy. Compd.*, 2009, **476**, 79-83.
31. A. D. Pelton, *Bull. Alloy Phase Diagr.*, 1987, **8**, 550-553.
32. Y. Pan, Y. Liu, G. Zeng, L. Zhao and Z. Lai, *Chem. Commun.*, 2011, **47**, 2071-2073.
33. S. Gadipelli, W. Travis, W. Zhou and Z. Guo, *Energy Environ. Sci.*, 2014, **7**, 2232-2238.
34. G. Kumari, K. Jayaramulu, T. K. Maji and C. Narayana, *J. Phys. Chem. A*, 2013, **117**, 11006-11012.
35. S. Chen, X. Li, E. Dong, H. Lv, X. Yang, R. Liu and B. Liu, *J. Phys. Chem. C*, 2019, **123**, 29693-29707.
36. Z.-S. Wu, W. Ren, L. Gao, B. Liu, C. Jiang and H.-M. Cheng, *Carbon*, 2009, **47**, 493-499.
37. C. Weidenthaler, A.-H. Lu, W. Schmidt and F. Schüth, *Micropor. Mesopor. Mater.*, 2006, **88**, 238-243.
38. L. G. Mar, P. Y. Timbrell and R. N. Lamb, *Thin Solid Films*, 1993, **223**, 341-347.
39. R. Al-Gaashani, S. Radiman, A. R. Daud, N. Tabet and Y. Al-Douri, *Ceram. Int.*, 2013, **39**, 2283-2292.
40. F. Tian, A. M. Cerro, A. M. Mosier, H. K. Wayment-Steele, R. S. Shine, A. Park, E. R. Webster, L. E. Johnson, M. S. Johal and L. Benz, *J. Phys. Chem. C*, 2014, **118**, 14449-14456.
41. Y. Aoi, K. Ono and E. Kamijo, *J. Appl. Phys.*, 1999, **86**, 2318-2322.
42. Q. Lai, Y. Zhao, Y. Liang, J. He and J. Chen, *Adv. Funct. Mater.*, 2016, **26**, 8334-8344.
43. K. Yan, Z. Lu, H.-W. Lee, F. Xiong, P.-C. Hsu, Y. Li, J. Zhao, S. Chu and Y. Cui, *Nat. Energy*, 2016, **1**, 16010.
44. H. Wang, J. Wu, L. Yuan, Z. Li and Y. Huang, *ACS Appl. Mater. Interfaces*, 2020, **12**, 28337-28344.
45. T.-S. Wang, X. Liu, X. Zhao, P. He, C.-W. Nan and L.-Z. Fan, *Adv. Funct. Mater.*, 2020, **30**, 2000786.
46. J. Kim, J. Lee, J. Yun, S. H. Choi, S. A. Han, J. Moon, J. H. Kim, J.-W. Lee and M.-S. Park, *Adv. Funct. Mater.*, 2020, **30**, 1910538.

47. I. Hasa, X. Dou, D. Buchholz, Y. Shao-Horn, J. Hassoun, S. Passerini and B. Scrosati, *J. Power Sources*, 2016, **310**, 26-31.

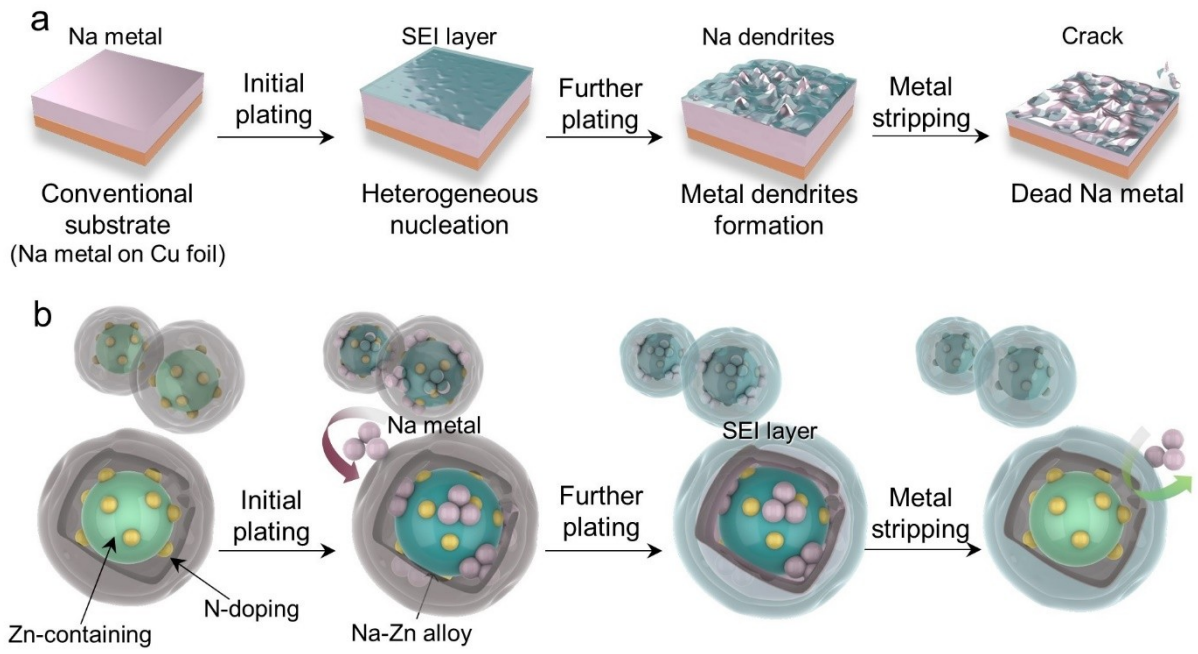

Fig. 1. Schematic illustration showing the Na deposition process on a conventional substrate and the Zn-containing porous carbon material: (a) On a conventional Cu electrode; the metal ions are heterogeneously distributed along the concentrated current flux at the defects on the electrode surface, causing a dendritic growth of the metal. (b) On the HZPC material; the metal ions are homogeneously regulated to undergo nucleation and grow at the high-nucleation-rate sites via the incorporation of metallic Zn clusters.

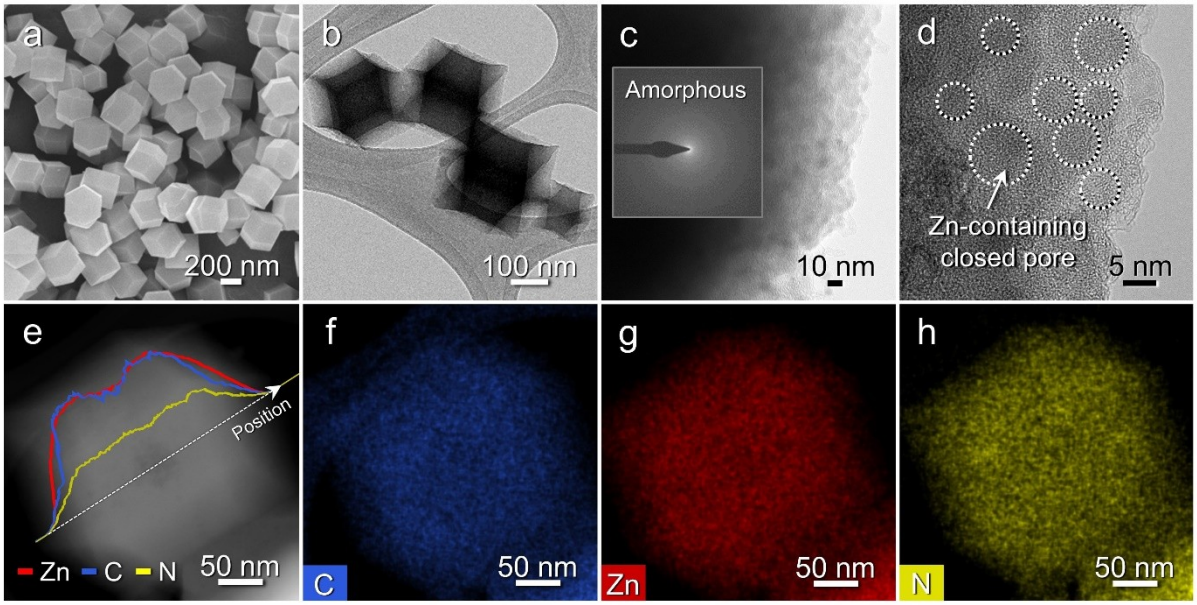

Fig. 2. Morphological characterization of HZPC: (a) Low-magnification FE-SEM image and (b) TEM image, (c, d) HR-TEM images showing its amorphous phase with Zn-containing closed pores, (e) EDS elemental line mapping result, and (f–h) EDS elemental mapping images for Zn, C, and N.

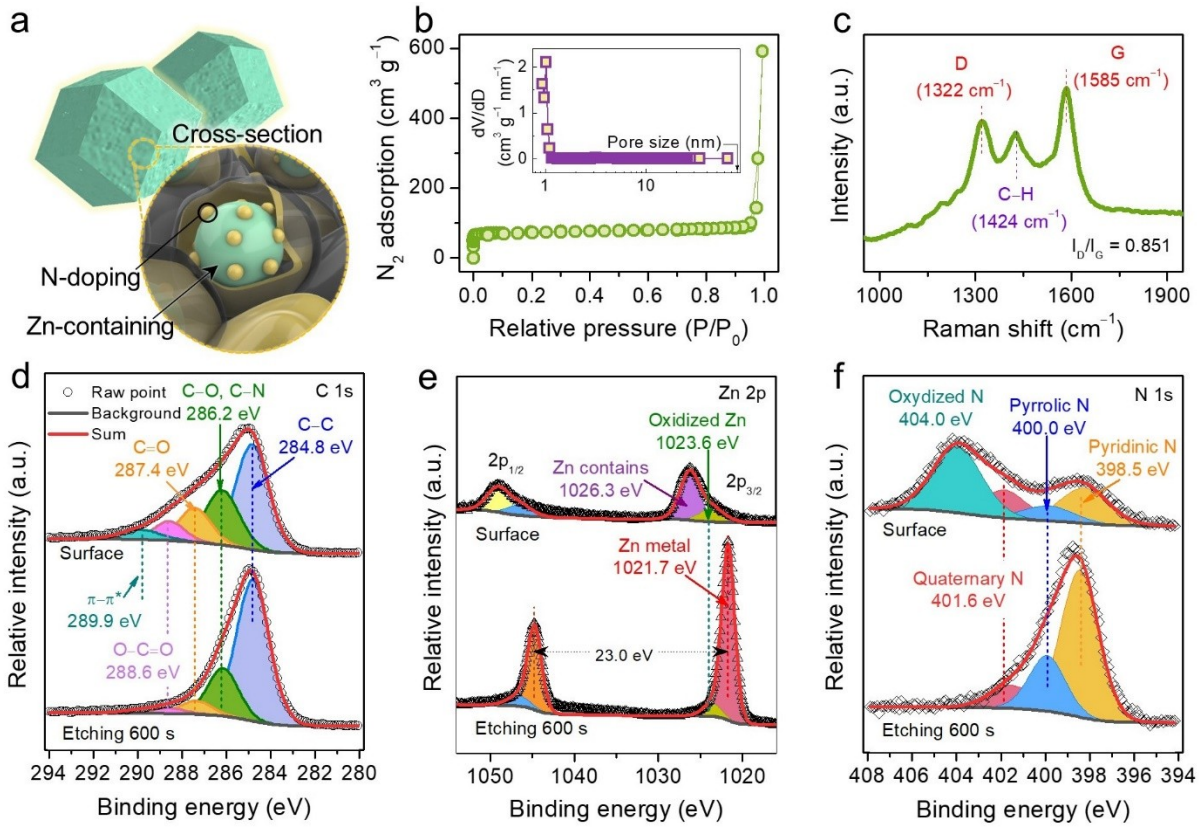

Fig. 3. (a) Simple schematic illustration of the Zn-containing porous carbon structure, (b) nitrogen adsorption-desorption isotherms and pore size distribution (inset), (c) Raman spectrum, and XPS core-level spectra for (d) Zn 2p, (e) C 1s, and (f) N 1s of HZPC.

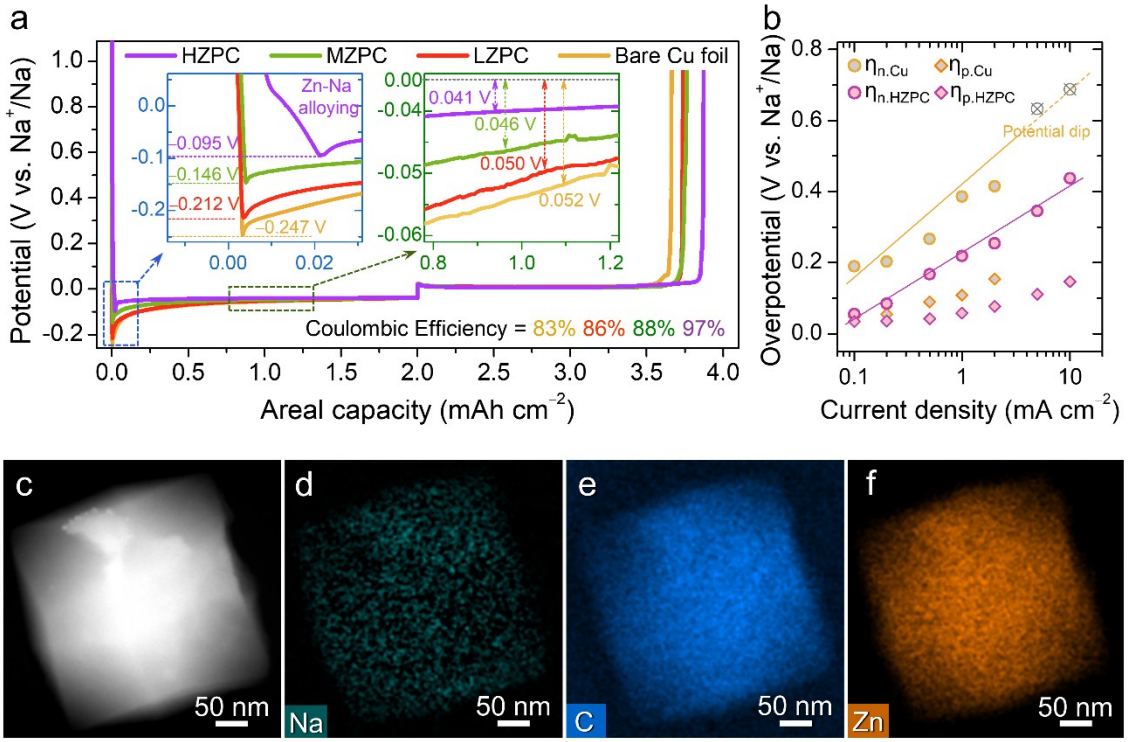

Fig. 4. (a) Galvanostatic voltage profiles obtained during the first Na plating/stripping at a current density of 0.1 mA cm^{-2} with a fixed areal capacity of 2.0 mAh cm^{-2} for all the Zn-containing porous carbon electrodes and bare Cu foil. (b) Overpotentials as a function of current density. (c–f) STEM image and EDS elemental mapping results for Na, C, and Zn.

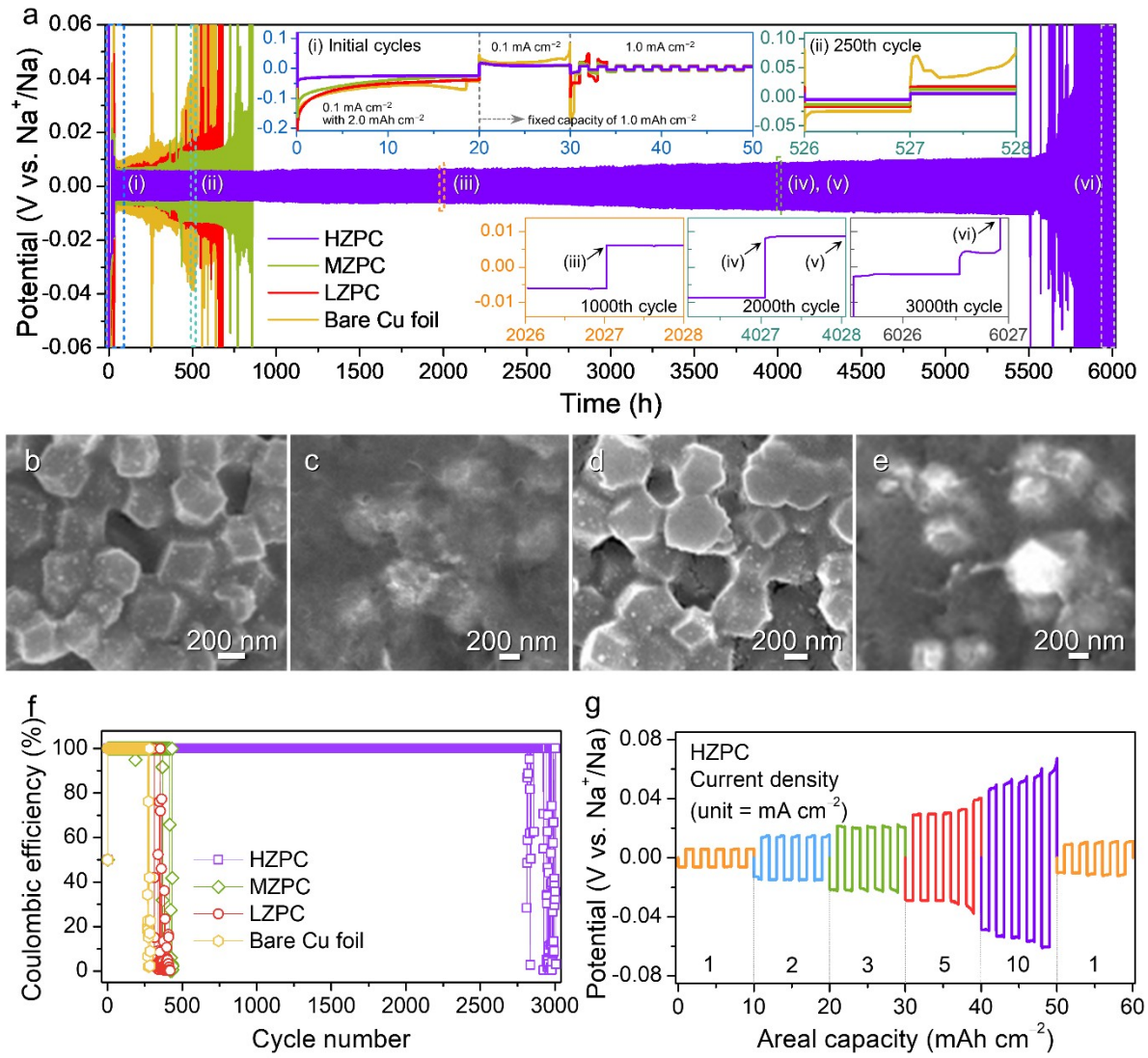

Fig. 5 Electrochemical performance comparison for all the Zn-containing porous carbon electrodes and bare Cu foil in the Na system: (a) Voltage profiles showing a stable cycle polarization at a current density of 1.0 mA cm^{-2} with a fixed capacity of 1.0 mAh cm^{-2}. The enlarged voltage profiles are presented in the inset. The initial cycles were performed at a current density of 0.1 mA cm^{-2}. Ex situ FE-SEM images obtained after the (b) 1000th deposition, (c) 2000th deposition, (d) 2000th dissolution, and (e) 3000th dissolution. (f) Cycle performance at a current density of 1.0 mA cm^{-2} and (g) rate performance of the HZPC electrode at various current densities of 1–10 mA cm^{-2}.

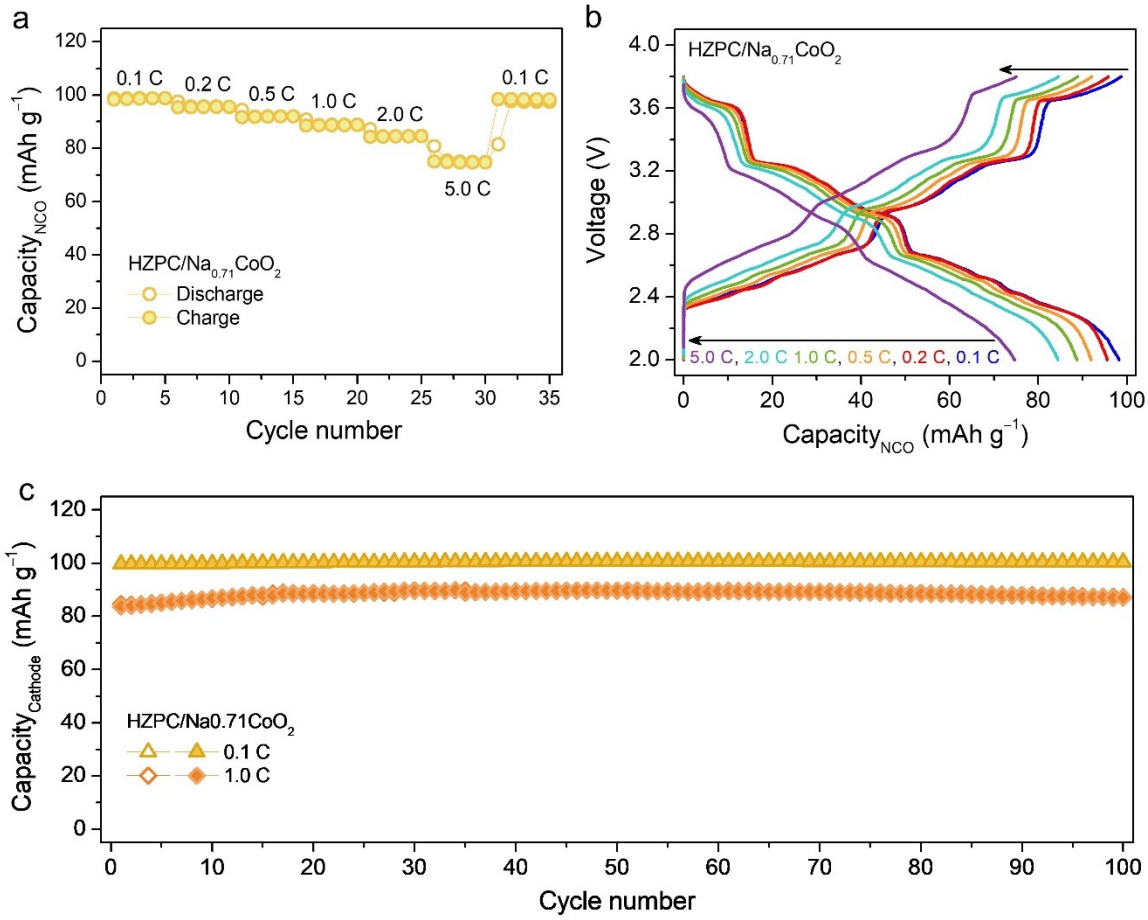

Fig. 6. Na full-cell test results (1 C = 100 mAh g^{-1}): (a) Rate performance at various current densities of 0.1–5.0 C, (b) voltage profiles, and (c) cycle performance of at the current densities of 0.1 and 1 C.